Wang *et al. Energy Mater.* **2025**, *5*, 500084
DOI: 10.20517/energymater.2024.251

Energy Materials

Article

Open Access

Check for updates

Tailoring crystal planes and oxygen vacancies of ceria for enhanced catalytic performance of single-atom Ru in hydrogenative dearomatization of lignin-derived phenols

Baoyu Wang[1,2], Ximing Yan[1,*], Ming Zhou[1], Hu Li[2,*]

[1]Guangxi Key Laboratory of Green Chemical Materials and Safety Technology, Beibu Gulf University, Qinzhou 535011, Guangxi, China.
[2]State Key Laboratory of Green Pesticide, Key Laboratory of Green Pesticide & Agricultural Bioengineering, Ministry of Education, State-Local Joint Laboratory for Comprehensive Utilization of Biomass, Center for R&D of Fine Chemicals, Guizhou University, Guiyang 550025, Guizhou, China.

[*]**Correspondence to:** Prof. Hu Li, State Key Laboratory of Green Pesticide, Key Laboratory of Green Pesticide & Agricultural Bioengineering, Ministry of Education, State-Local Joint Laboratory for Comprehensive Utilization of Biomass, Center for R&D of Fine Chemicals, Guizhou University, 2708 South Section of Huaxi Avenue, Huaxi District, Guiyang 550025, Guizhou, China. E-mail: hli13@gzu.edu.cn; Dr. Ximing Yan, Guangxi Key Laboratory of Green Chemical Materials and Safety Technology, Beibu Gulf University, 12 Binhai Avenue, Binhai New Town, Qinzhou 535011, Guangxi, China. E-mail: yanximing123456@163.com

How to cite this article: Wang, B.; Yan, X.; Zhou, M.; Li, H. Tailoring crystal planes and oxygen vacancies of ceria for enhanced catalytic performance of single-atom Ru in hydrogenative dearomatization of lignin-derived phenols. *Energy Mater.* **2025**, *5*, 500084. https://dx.doi.org/10.20517/energymater.2024.251

Received: 13 Nov 2024 **First Decision:** 6 Jan 2025 **Revised:** 26 Jan 2025 **Accepted:** 20 Feb 2025 **Published:** 21 Apr 2025

Academic Editor: Ho Won Jang **Copy Editor:** Ping Zhang **Production Editor:** Ping Zhang

Abstract

Lignin-based guaiacol and its derivatives can be hydrogenated to synthesize 2-methoxycyclohexanols (2-MCHs), widely used in the pharmaceutical industry, while the efficient catalytic conversion of guaiacols into 2-MCHs is challenging due to the interference of the side reaction of C_{Ar}-OCH_3 bond cleavage. In this work, highly selective hydrogenation of various guaiacyl lignin-derived phenols to 2-MCHs (yields of 86%-97%) was realized over a single-atom Ru-based catalyst (Ru_1/*o*-CeO_2-ov) that preferentially exposes the CeO_2(111) plane and has abundant oxygen vacancies. Control experiments and mechanism studies expounded that Ru-O-Ce is the active site for hydrogenation of aromatic ring in guaiacols, and the exposed (111) plane and abundant oxygen vacancies of ceria can reduce the activation energy of aromatic ring hydrogenation, thereby enabling guaiacols to generate the corresponding hydrogenated products with high selectivity. Response surface optimization experiments indicated that temperature and time have relatively more significant effects on the 2-MCH yield. Moreover, the Ru_1/*o*-CeO_2-ov catalyst exhibited excellent reusability, and was extensively applicable to the hydrogenative

dearomatization of different types of lignin-derived phenols, providing a unique solution for upgrading biomass feedstock into specific structural chemicals.

Keywords: Single-atom catalyst, lignin-derived phenols, oxygen vacancy, crystal plane control, aromatic ring hydrogenation

INTRODUCTION

Catalytic upgrading of lignin-based renewable resources into high-value-added chemicals and biofuels will bring enormous social and economic benefits to humankind, which has also been the focus of researchers in recent years[1]. As an essential class of lignin phenols, guaiacol and its derivatives can be converted into catechols[2], phenols[3], cyclohexanols[4,5], ethers[6,7], arenes[8,9], cyclohexanes[10], *etc.*, through selective cleavage of C-O bond and/or hydrogenation of benzene ring[11]. Notably, the aromatic ring hydrogenation of guaiacols can produce 2-methoxycyclohexanols (2-MCHs), which have both hydroxyl (-OH) and ether (C_6H_{10}-O-CH_3) bonds and are often used as excellent solvents in the chemical industry[12]. In particular, the six-membered ring skeleton of cyclohexane has a unique chiral structure, making it have outstanding application value in synthesizing antibacterial drugs, bioactive molecules, and chiral auxiliary agents[13]. However, the current method for the synthesis of 2-MCH mainly relies on the reaction of fossil energy-based cyclohexene oxide and methanol[14-17], which does not meet the requirements of sustainable development [Scheme 1A][18].

Typically, the C_{Ar}-OCH_3 cleavage of guaiacols is directly competitive with the aromatic ring hydrogenation reaction[19,20], which depends on the identity of the active hydrogen (H* and H^+), the isomerization equilibrium of ketene and alcohol, and the transition state barrier of the C_{Ar}-OCH_3 cleavage[21]. In previous studies, the intramolecular hydrogen bonds formed by guaiacol were illustrated to preferentially undergo C_{Ar}-OCH_3 cleavage over Co-based catalysts[22]. The ring hydrogenation in guaiacol was found to be faster than C_{Ar}-OCH_3 cleavage from the perspective of transition state energy, but the latter was more likely to occur from a microdynamic analysis, possibly due to the considerable interaction between the benzene ring on guaiacol and the catalyst[23]. In addition, 2-MCHs were inclined to complete the demethoxylation reaction under certain conditions, resulting in the final production of cyclohexanols rather than 2-MCHs[24]. It can thus be seen that promoting the hydrogenation of the aromatic ring while preserving the C-OCH_3 ether bonds is the challenge faced in the highly selective conversion of guaiacols to 2-MCHs. A theoretical study suggested that changing the metal properties of the catalyst could change the reaction route of guaiacol and improve the selectivity of 2-MCHs[21]. By designing a closed nano-Ni-based catalyst, the hydrogen coverage could be effectively increased so that guaiacol was converted entirely with a 2-MCH yield of more than 95%[25]. However, these highly dispersed Ni nanoparticles (NPs) are unstable, and a hydrogen reduction step must be added every time they are recycled [Scheme 1B]. Rh/C catalyst could hydrogenate guaiacol under harsh conditions of supercritical CO_2, obtaining 2-MCH in 95.5% yield[26]. The other studies further expanded the ruthenium (Ru)-based catalysts for conventional benzene ring hydrogenation to 2-MCH, but due to the dual constraints of kinetics and thermodynamics, either the product yield was low (48%) or a long reaction time (5-48 h) was required[27-30]. Therefore, constructing suitable catalytic systems to quickly and efficiently convert lignin-derived phenols into the corresponding 2-MCHs remains an urgent issue to resolve.

Over the past decade, single-atom catalysts (SACs) have shown high catalytic performance in many reactions due to the isolated atoms being more easily affected by metal oxides to change their *d*-band center position and *d*-band width[31-33]. However, due to the lack of metal bonds and weak hydrogen spillover

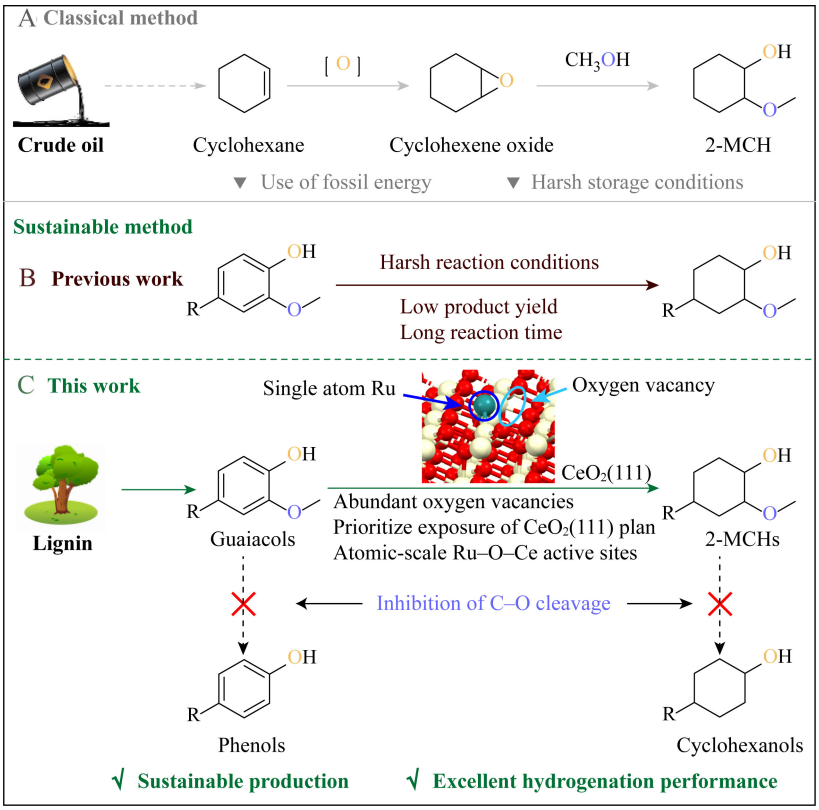

Scheme 1. Synthesis methods of 2-MCHs. Classical method (A) and sustainable method in previous work (B) and this work (C). 2-MCHs: 2-methoxycyclohexanols.

performance, it is difficult for SACs to complete the hydrogenation of benzene rings with comparable efficiency to traditionally supported metal NPs[24,34]. SACs have been developed for the upgrading of vanillin, among which Co-based SAC [Co_1@NC-(SBA)] can promote the hydrodeoxygenation of vanillin to 4-methylguaiacol[35]. In subsequent studies, Ni-based SACs were used to remove oxygen from the aldehyde group of vanillin using methanoic acid as a hydrogen donor[36]. However, these SACs could not catalyze the cleavage of C_{Ar}-OCH_3 bonds and the saturation of aromatic rings. The noble metal catalysts prepared by loading Au and Pt single atoms onto WO_{3-x} and TiO_2, respectively, were reported to have excellent demethoxylation ability, which could convert 4-propylguaiacol into 4-propylphenol with high selectivity, but did not show activity for aromatic ring hydrogenation[34]. Zhang *et al.* first reported that Ru SACs could hydrogenate aromatic rings when studying the selective hydrogenation of guaiacol. Unfortunately, the conversion process not only saturates the aromatic ring but also promotes the selective cleavage of the C-O bond, resulting in the product being almost cyclohexanol rather than 2-MCH[24]. Benefiting from the electronic properties and acidity of the support, the Ni_1/β-Mo_2C and $Pt_{0.4}$/CsPW-H_2 catalysts could complete the hydrodeoxygenation of lignin-derived phenols while hydrogenating the aromatic rings to produce cycloalkanes[37,38]. In this context, the complete aromatic ring hydrogenation of biomass-derived guaiacols to 2-MCHs catalyzed by SACs while suppressing the selective cleavage of the C_{Ar}-OCH_3 bond remains challenging.

Here, a Ru-based SAC (Ru_1/*o*-CeO_2-ov) with exposed crystal planes and oxygen vacancies of ceria was precisely constructed, which could completely hydrogenate the aromatic ring while suppressing the C_{Ar}-OCH_3 bond cleavage of guaiacols, thereby efficiently synthesizing 2-MCHs [Scheme 1C]. Mechanism

studies and control experiments jointly pointed to Ru-O-Ce as the active site for aromatic ring hydrogenation. Forming the CeO_2(111) plane and oxygen vacancies could reduce the transition state energy barrier for aromatic ring hydrogenation. The higher C_{Ar}-OCH_3 cleavage barrier at the Ru_1/*o*-CeO_2-ov site illustrated that guaiacol could be hydrogenated to 2-MCH with high selectivity. The response surface optimization was able to achieve a 2-MCH yield of over 97% and the Ru_1/*o*-CeO_2-ov catalyst exhibited excellent aromatic ring hydrogenation performance for a wide range of lignin-derived phenols and real lignin oil. The results confirm the important role of crystal plane effect and oxygen vacancies of Ru-based SACs in selective aromatic ring hydrogenation, offering a unique solution for upgrading and transforming raw biomass materials into specific structural chemicals.

EXPERIMENTAL

Materials

Cerous nitrate hexahydrate (99%), sodium hydroxide (99%), sodium orthophosphate (98%), ruthenium trichloride hydrate (99.95% metals basis), cobalt nitrate hexahydrate (99.99% metals basis), copper(ii) nitrate hydrate (99.99% metals basis), ferric nitrate nonahydrate (99.99% metals basis), nickel(II) chloride hexahydrate (99.9%), phenol (99.5%), guaiacol (98%), 4-methylphenol (99%), 4-methylguaiacol (99%), 4-ethylphenol (97%), 4-ethylguaiacol (99%), 4-propylphenol (99%), 4-propylguaiacol (99.5%), 2,6-dimethoxyphenol (98%), octane (99%), and hexadecane (99%) were purchased from Aladdin (Shanghai, China) Biochemical Technology Co., ltd. The real lignin oil was derived from reductive catalytic fractionation of birch wood (Alibaba).

Catalyst preparation

Preparation of SACs

The preparation methods of ceria support with different morphologies (*x*-CeO_2) are shown in the Supporting information. A series of SACs were prepared by loading metal ions onto *x*-CeO_2 using the supersaturated impregnation method. In a typical example, 100 mg octahedral ceria (*o*-CeO_2) was dispersed in 20 mL deionized water, and then an aqueous solution containing 2.0 mg hydrated ruthenium trichloride was added dropwise to the dispersion. The resulting mixed turbid liquid was stirred at 25 °C for 6 h, and the Ru_1/*o*-CeO_2 catalyst was obtained after washing, centrifugation, and vacuum drying (80 °C). Next, Ru_1/*c*-CeO_2 and Ru_1/*r*-CeO_2 SACs could be prepared by changing the morphology of ceria. Finally, 3*d* transition metals were selected using the same preparation method to obtain a series of SACs M_1/*o*-CeO_2, where *M* represents Co, Ni, Cu, and Fe, respectively.

Preparation of Ru_1/x-CeO_2-ov

Oxygen vacancies were introduced into Ru-based SACs by a high-temperature reduction method. The typical process for preparing Ru_1/*x*-CeO_2-ov was to place 100 mg of Ru_1/*x*-CeO_2 in a tube furnace. In a 10% H_2/Ar atmosphere, the temperature was increased from 30 °C to 400 °C (rate of 5 °C min^{-1}) and kept constant for 3 h. Then, the temperature was reduced to 100 °C (rate of 5 °C min^{-1}), and the program was stopped. The sample was taken out when it was cooled down to below 30 °C for use.

Catalyst characterization

The X-ray diffraction (XRD) patterns and Raman spectra of the samples were obtained using Bruker's D8 ADVANCE X-ray powder diffractometer and HORIBA's LabRam HR Evolution, respectively. The elements of the samples were quantitatively analyzed using a PE Optima 8000 inductively coupled plasma optical emission spectrometer (ICP-OES) from PerkinElmer, USA. X-ray photoelectron spectroscopy (XPS) of all samples was measured by ESCALAB 250XI instrument from Thermo. The microstructure, elemental composition, and distribution of the samples were analyzed using a scanning transmission electron microscope (STEM) combined with an energy-dispersive X-ray spectrometer (EDS). Atomic mapping of

the sample was collected using an aberration-corrected high-angle annular dark field STEM (AC HAADF STEM, JEOL ARM 200F) equipped with a Cs corrector (JEM-2200FS) and a high-resolution spectrometer with a large solid angle of 0.97 sr (JED-2300T). The acceleration voltage was 200 kV, the STEM probe current was 17 pA, and the probe size was 0.133 nm. Surface area and pore size distribution were determined using a Micromeritics ASAP2460 apparatus. The hydrogen temperature-programmed reduction (H_2-TPR) curves were obtained on an AutoChem II 2920 instrument. The characteristics of oxygen vacancies in the samples were analyzed using a Bruker ELEXSYS E500 electron paramagnetic resonance (EPR) spectrometer.

Catalyst activity evaluation and first-principles calculations

Model molecule experiments

The hydrogenation reactions of lignin-derived phenolic model molecules were carried out in a high-pressure reactor (25 mL) equipped with a magnetic stirrer. In a typical example, 1 mmol of guaiacol, 3 mL of *n*-octane (solvent), 0.3 mol% Ru_1/o-CeO_2-ov catalyst, and 20 mg of *n*-hexadecane as an internal standard were added to the autoclave. The products were qualitatively analyzed using an Agilent 5,977 A gas chromatograph-mass spectrometer (GC-MS), and quantitatively analyzed using an Agilent 7,890 A gas chromatograph (GC) equipped with a hydrogen flame ionization detector and an HP-5 capillary column (30 m × 0.25 mm × 0.25 μm). The catalyst activity evaluation indexes include guaiacol conversion (Conv.), 2-MCH selectivity (Sel.), and 2-MCH yield, which were calculated according to

$$\text{Conv.} = {(n_1 - n_2)}/{n_1} \times 100\% \quad (1)$$

$$\text{Sel.} = {n_3}/{(n_1 - n_2)} \times 100\% \quad (2)$$

$$\text{Sel.} = {n_3}/{n_1} \times 100\% \quad (3)$$

Where n_1 is the molar amount of the initial substrate, n_2 is the molar amount of the remaining substrate, and n_3 is the molar amount of 2-MCHs generated. In addition, to compare the activity of catalysts with those in the literature, the turnover frequency (TOF) of this work was calculated according to

$$\text{TOF}\left(\text{h}^{-1}\right) = \frac{\text{Molar amount of 2-MCH generated}}{\text{Reaction time (h)} \times \text{Molar amount of active metal}} \quad (4)$$

Real lignin oil experiment

The hydrogenation of real lignin oil was also carried out in a high-pressure reactor equipped with a magnetic stirrer. The specific operation steps were to add 150 mg of lignin oil, 3 mL of *n*-octane, and 100 mg of Ru_1/o-CeO_2-ov catalyst into the reactor. Then, the lignin oil was hydrogenated at 200 °C and 3 MPa H_2 for 48 h. The product after the reaction was filtered through a 0.22 μm organic filter membrane, and the solvent was removed by rotary evaporation and then analyzed by two-dimensional (2D) heteronuclear single quantum coherence nuclear magnetic resonance (2D HSQC NMR) spectroscopy with deuterated dimethyl sulfoxide (DMSO).

Theoretical calculations

Density functional theory (DFT) calculations were performed in this work using the Vienna ab initio simulation package (VASP) software. The calculation details are given in the Supplementary Materials.

RESULTS AND DISCUSSION

Catalyst preparation and characterization

The preparation process of octahedral (*o*-CeO_2), cubic (*c*-CeO_2), and rod-shaped (*r*-CeO_2) ceria is shown in Figure 1A. XRD patterns confirmed that the characteristic diffraction peaks of the three carriers all belong to CeO_2 crystals with face-centered cubic structure (PDF# 43-1002) [Supplementary Figure 1]. Transmission electron microscopy (TEM) images showed that the supports *o*-CeO_2, *c*-CeO_2, and *r*-CeO_2 corresponded to octahedral, cubic, and rod-shaped crystal morphologies, respectively [Supplementary Figures 2-4]. Each face on *o*-CeO_2 and *c*-CeO_2 had the same crystal face cluster, corresponding to {111} and {100}, respectively, which indicated that *o*-CeO_2 and *c*-CeO_2 were prone to expose the (111) and (100) planes[39]. The supersaturated impregnation and hydrogen reduction method was adopted to prepare a series of Ru-based SACs (Ru_1/*x*-CeO_2-ov) based on three CeO_2 supports with different morphologies [Figure 1A]. The catalysts introduced with single-atom Ru still maintained the crystalline structure of ceria [Supplementary Figure 5]. The EDS images displayed that the metal Ru on the catalysts Ru_1/*x*-CeO_2-ov was evenly dispersed on the carrier [Figure 1B-D]. ICP-OES results showed that the mass fraction of Ru in the above four catalysts was between 0.287%-0.541%, and the lower loading amount of Ru could be better dispersed on the surface of the ceria [Table 1]. P and Cl element signals were not detected by ICP, indicating that these elements could be removed by water washing and hydrogen pre-reduction. Similarly, the characteristic peaks of P and Cl were not observed in the EDS spectra of Ru_1/*x*-CeO_2-ov [Supplementary Figures 6-8]. In addition, since the EDS energy spectrum could only observe the element content near the surface of the catalyst, the Ru content tested by EDS was much higher than the result of ICP-OES [Table 1], which confirmed that Ru was more loaded on the surface of the ceria support. High-resolution TEM images could further observe that the catalysts prepared with three morphologies of *x*-CeO_2 carriers all had visible lattice patterns [Figure 1E-G]. Fast Fourier transform (FFT) of the lattice patterns further confirmed that Ru_1/*o*-CeO_2-ov and Ru_1/*c*-CeO_2-ov preferentially exposed the (111) and (100) planes of CeO_2, respectively, while Ru_1/*r*-CeO_2-ov mainly exposed the (110) and (100) planes (insets of Figure 1E-G). The atomic-level EDS energy spectrum of Ru_1/*o*-CeO_2-ov under AC HAADF STEM was revealed in Figure 1H and Supplementary Figure 9. Although some blue signals representing Ru atoms overlap with the red signals of Ce atoms, it could still be intuitively found that the Ru atoms were isolated, verifying that the metallic Ru was loaded on the surface of the *o*-CeO_2 carrier in the form of a single atom. The absence of green signals representing oxygen atoms in some areas suggested the generation of oxygen vacancies on the Ru_1/*o*-CeO_2-ov surface. The results of nitrogen adsorption and desorption characterization showed that the specific surface area of the catalyst was 5.35-61.34 $m^2 g^{-1}$ [Table 1]. Due to the smaller size of Ru_1/*r*-CeO_2-ov, it had the largest specific surface area, which was consistent with the full width at half maximum (FWHM) in the XRD patterns. The pore size distribution showed that Ru_1/*x*-CeO_2-ov accumulates some mesopores, which may help the substrate diffuse to the active sites for reaction [Supplementary Figure 10]. In addition, in the Raman spectra of Ru_1/*o*-CeO_2-ov, Ru_1/*c*-CeO_2-ov, and Ru_1/*r*-CeO_2-ov, no bands attributable to RuO_2 were detected at 528 cm^{-1}, 646 cm^{-1}, and 716 cm^{-1}[40]. However, the band at 980 cm^{-1} was assigned to the vibration of the Ru-O-Ce bond, which was not detected in *o*-CeO_2, indicating that the metal Ru was in a single-atom dispersed state and forms a Ru-O-Ce bond with the carrier [Supplementary Figure 11][41]. At the same time, no signal peak attributed to Ru-Ru appeared in the Ru 3*p* XPS fitting of the Ru_1/*o*-CeO_2-ov catalyst [Supplementary Figure 12], which means that there is no agglomeration of metallic Ru on the catalyst surface, consistent with the EDS mapping [Figure 1H].

The oxygen vacancies in ceria can regulate the electronic structure of active metals, change the charge transfer ability of the material, and thus improve the catalyst performance[42]. H_2-TPR results showed that the Ru_1/*x*-CeO_2-ov sample had two obvious reduction peaks, in which the first peak (α, ca. 100 °C) can be attributed to the reduction of Ru on the Ru-O-Ce site, while the second peak (β, 150-300 °C) may come from the reduction caused by the embedding of Ru atoms into the CeO_2 lattice [Figure 2A]. Notably, the H_2

Table 1. Catalyst characterization results

Catalyst	Ru content (wt%)		S_{BET} ($m^2 g^{-1}$)[a]	FWHM (°)	Hydrogen consumption ($\mu mol\ g^{-1}$)[b]	
	ICP-OES	EDS			α	β
$Ru_1/o\text{-}CeO_2$-ov	0.287	1.26	7.22	0.21	63.7	75.6
$Ru_1/c\text{-}CeO_2$-ov	0.452	1.35	5.35	0.15	52.6	103.6
$Ru_1/r\text{-}CeO_2$-ov	0.541	1.88	61.34	0.61	86.4	246.1

[a] BET surface area. [b] H_2-TPR. ICP-OES: Inductively coupled plasma optical emission spectrometer; EDS: energy-dispersive X-ray spectrometer.

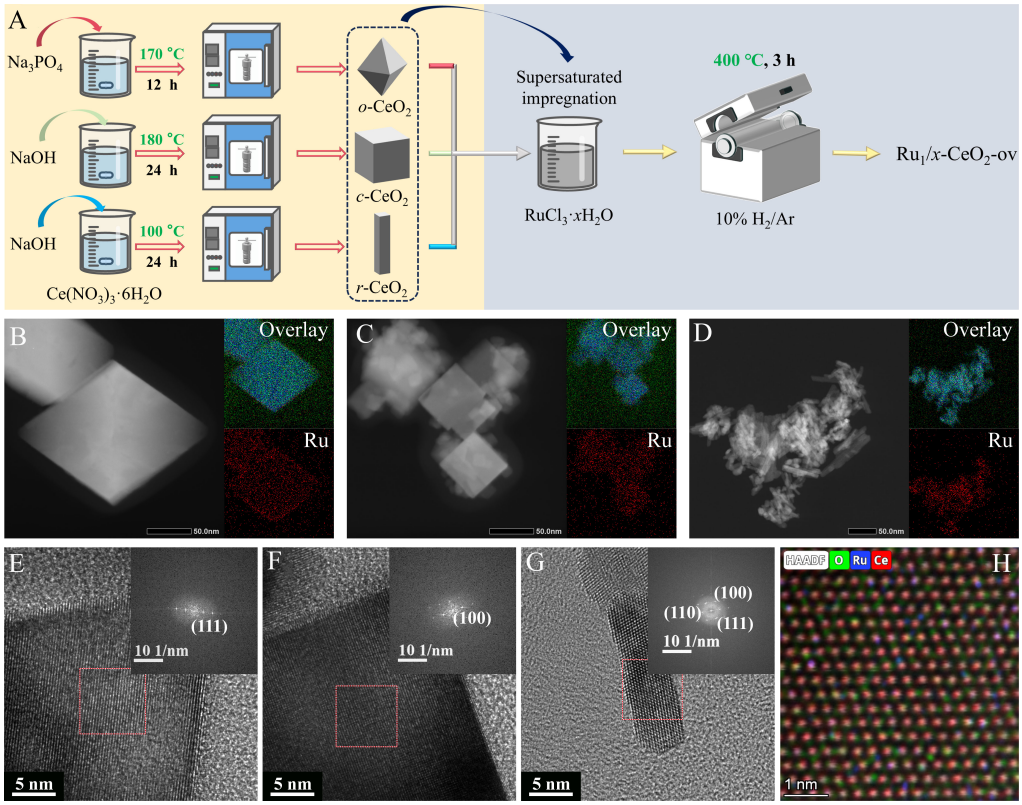

Figure 1. (A) Schematic diagram of the preparation process of Ru-based catalysts supported on ceria of different morphologies; (B-D) HAADF STEM images and EDS elemental mappings of $Ru_1/o\text{-}CeO_2$-ov, $Ru_1/c\text{-}CeO_2$-ov, and $Ru_1/r\text{-}CeO_2$-ov; (E-G) High-resolution TEM images of $Ru_1/x\text{-}CeO_2$-ov (inset is FFT images); (H) AC HAADF STEM EDS mapping of the $Ru_1/o\text{-}CeO_2$-ov catalyst. AC HAADF STEM: Aberration-corrected high-angle annular dark field scanning transmission electron microscope; EDS: dispersive X-ray spectrometer; TEM: transmission electron microscopy.

consumption of the α and β peaks was much greater than that required for the reduction of Ru-O-Ce due to the lower Ru loading [Table 1]. A generally accepted explanation is that introducing Ru causes strong metal-support interactions, which leads to the transfer of electrons from Ru to ceria, thereby promoting the continuous reverse spillover of oxygen in ceria to Ru[43]. In a hydrogen atmosphere, oxygen atoms diffuse from the CeO_2 bulk to the surface, and the effect of Ru metal accelerates the oxygen spillover process. The water generated by the combination of oxygen and hydrogen will escape from the catalyst surface after exceeding 300 °C, resulting in the appearance of oxygen vacancies[44]. The higher oxygen mobility caused by the Ru-O-Ce bond could dynamically form more oxygen vacancies and efficiently complete the catalytic reaction.

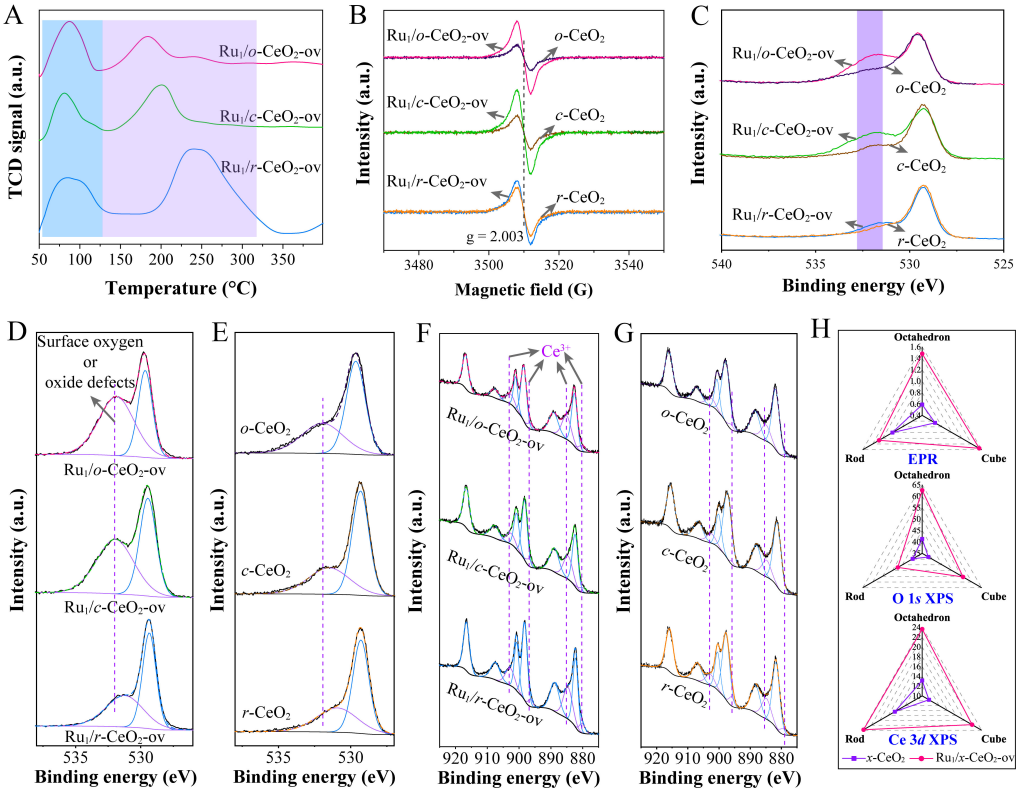

Figure 2. (A) H_2-TPR curves of Ru_1/o-CeO_2-ov, Ru_1/c-CeO_2-ov, and Ru_1/r-CeO_2-ov. EPR (B) and O 1s XPS (C) spectra of x-CeO_2 and Ru_1/x-CeO_2-ov. Deconvoluted O 1s XPS spectra of Ru_1/x-CeO_2-ov (D) and x-CeO_2 (E); Deconvoluted Ce 3*d* XPS spectra of Ru_1/x-CeO_2-ov (F) and x-CeO_2 (G); (H) Comparison of relative oxygen vacancy contents of Ru_1/x-CeO_2-ov and x-CeO_2. H_2-TPR: Hydrogen temperature-programmed reduction; EPR: electron paramagnetic resonance; XPS: X-ray photoelectron spectroscopy.

From the EPR characterization results of x-CeO_2 and Ru_1/x-CeO_2-ov samples, it can be seen that all samples exhibited an EPR signal with a g value of about 2.003 [Figure 2B]. Considering the elemental composition of the catalyst, it is suggested that the signal with a g value of 2.003 represents the presence of oxygen vacancies. Compared with the x-CeO_2 carriers, the oxygen vacancy signal intensity of the Ru_1/x-CeO_2-ov series samples increased, especially the signal intensity of Ru_1/o-CeO_2-ov and Ru_1/c-CeO_2-ov samples increased by more than twice. It is worth noting that due to the low crystallinity of r-CeO_2, it contains more oxygen vacancies, which only increases the oxygen vacancy concentration of the catalyst (Ru_1/r-CeO_2-ov) by 60% after introducing Ru. Consistent with the EPR detection results, the O 1*s* XPS spectra of x-CeO_2 and Ru_1/x-CeO_2-ov could more intuitively show that introducing Ru atoms increases the oxygen vacancy concentration of ceria [Figure 2C]. After deconvolution of the O 1*s* XPS spectrum, two characteristic peaks at ca. 531.8 eV and ca. 529.5 eV could be decomposed [Figure 2D and E]. The former corresponds to low-coordinated oxidation defects, surface oxygen ions, hydroxyls or carbonates, and the latter belongs to lattice oxygen. It can be seen that the relative contents of the peak at the binding energy of 531.8 eV for Ru_1/o-CeO_2-ov, Ru_1/c-CeO_2-ov, and Ru_1/r-CeO_2-ov catalysts increased from 41%, 38%, and 40% of the original ceria to 62%, 55%, and 47%, respectively. The preparation conditions of the three morphologies of x-CeO_2 or Ru_1/x-CeO_2-ov are consistent, which makes us believe that low-coordinated oxygen species mainly cause changes in the binding energy position peak. The increase in Ce^{3+} content in Ce 3*d* XPS could also be used to confirm the formation of oxygen vacancies. Since the electronic structure of Ce 3*d* orbital was affected by the hybridization of Ce 4*f* and O 2*p* orbital valence bands, the four peaks with binding energies near 880.2 eV, 885.2 eV, 896.7 eV, and 903.1 eV among the ten characteristic peaks decomposed

after deconvolution of Ce 3*d* XPS spectrum were all contributed by Ce^{3+} [Figure 2F and G]. The six peaks with binding energies of 882.0 eV, 888.3 eV, 897.8 eV, 900.5 eV, 906.7 eV, and 916.0 eV all resulted from Ce^{4+}. Compared with the *x*-CeO_2 support, the higher Ce^{3+} concentration in the Ru_1/*x*-CeO_2-ov samples further confirmed that more surface oxygen vacancies could be obtained by introducing atomic-level Ru and hydrogen reduction. In summary, it was found from the results of EPR, O 1*s* XPS, and Ce 3*d* XPS that the introduction of Ru could effectively increase the concentration of oxygen vacancies on the catalyst surface, among which Ru_1/*o*-CeO_2-ov had the most significant increase [Figure 2H].

Catalyst performance evaluation

Initially, guaiacol (**1a**) was used as a model compound to undergo hydrogenative dearomatization to synthesize 2-MCH (**2a**) over different catalysts at 100 °C and 3 MPa H_2 for 3 h [Table 2]. It was observed that none of the three ceria supports (*x*-CeO_2) performed aromatic ring hydrogenation (entries 1-3 in Table 2). It is worth noting that the Ru-based SACs (Ru_1/*x*-CeO_2) obtained based on ceria supports (*x*-CeO_2) with different morphologies all showed high **2a** selectivity (80.9%-94.8%) (entries 4-6 in Table 2), probably due to the Ru-O-Ce bond formed between single atom Ru and CeO_2. However, the M_1/*o*-CeO_2 series of SACs composed of 3*d* transition metals (Co, Ni, Cu, and Fe) also failed to achieve the hydrogenation reaction of **1a** (entries 7-10 in Table 2), indicating that the M-O-Ce bonds formed by these four 3*d* transition metals could not activate the aromatic ring within the experimental range of this work. In addition, compared to Ru_1/*x*-CeO_2, the Ru_1/*x*-CeO_2-ov series catalysts reduced by hydrogen achieved higher **1a** conversion while maintaining the **2a** selectivity, indicating that the oxygen vacancies on the catalysts could significantly improve the aromatic ring hydrogenation activity (entries 11-13 in Table 2). In a comparison of the hydrogenation dearomatization activities of three morphological Ru_1/*x*-CeO_2-ov catalysts, it was found that **1a** was almost wholly converted on Ru_1/*o*-CeO_2-ov, and the yield for **2a** reached 96.3% (entry 11), which was significantly higher than that of Ru_1/*c*-CeO_2-ov and Ru_1/*r*-CeO_2-ov (entries 12 and 13), suggesting that the Ru-O-Ce sites formed on the most thermodynamically stable (111) plane of ceria were more accessible to activate the aromatic rings in guaiacol. Therefore, Ru_1/*o*-CeO_2-ov prepared by *o*-CeO_2 loaded with single atom Ru preferentially exposed the CeO_2(111) plane, had rich oxygen vacancies, and formed Ru-O-Ce active sites that could hydrogenate **1a** to **2a** of high selectivity.

The reaction network of **1a** was investigated by adjusting the reaction conditions and controlling the experiments using Ru_1/*o*-CeO_2-ov catalyst. First, when the reaction temperature reached 100 °C, **1a** could be almost wholly converted, indicating that the reaction was in the kinetic control range below 100 °C [Figure 3A]. As an intermediate, **2a** would further undergo demethoxylation reaction to give **3a** (Route **1**), and the **1a** conversion was accelerated with increasing temperature due to kinetics. Under a hydrogen pressure of 1 MPa, the conversion rate of **1a** was only 70.7%, while **1a** could be completely converted when the hydrogen pressure reached 3 MPa [Figure 3B]. A credible reason is that the increase in hydrogen pressure can increase the hydrogen coverage of the catalyst surface, thereby promoting the hydrogenation of **1a**. It is worth noting that after the hydrogen pressure exceeded 3 MPa, further increasing the pressure would lead to a decrease in the yield of **2a** and an increase in the yield of **3a**, illustrating the conversion of **2a** to **3a**. Next, the effect of time on the product yield showed that even if **1a** had been completely reacted, **3a** would continue to increase with the extension of reaction time, further verifying that **2a** was an intermediate product of the reaction [Figure 3C]. Although **2a** could undergo a C-O bond cleavage reaction, the presence of phenol intermediate was not detected using gas chromatography, resulting in the inability to determine whether **1a** undergoes a C_{Ar}-OCH_3 bond cleavage reaction to generate **3a** via Route **2** under experimental conditions. In addition, the extrapolated initial reaction rate (r_I) could better evaluate the difficulty of each step in the reaction network of **1a**, and given that the conversion of **2a** to **3a** was a slow process, the average reaction rate (r_A) could be used instead of r_I. It can be seen that the r_I of **1a** was 0.318 mol L^{-1} h^{-1}, which is 54 times higher than that of **2a** [Supplementary Figure 13], indicating that the

Table 2. Catalytic hydrogenative dearomatization of 1a to 2a with different catalysts

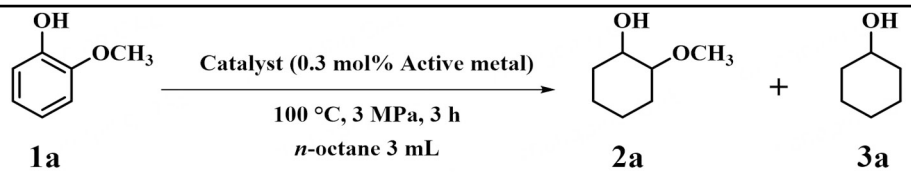

1a 2a 3a

Entry	Catalyst	Conv. of 1a (%)	Sel. of 2a[a] (%)	Yield of 2a (%)
1[b]	*o*-CeO_2	-	-	-
2[b]	*c*-CeO_2	-	-	-
3[b]	*r*-CeO_2	-	-	-
4	Ru_1/*o*-CeO_2	30.7	94.8	29.1
5	Ru_1/*c*-CeO_2	24.2	85.5	20.7
6	Ru_1/*r*-CeO_2	28.1	80.9	22.7
7	Co_1/*o*-CeO_2	-	-	-
8	Ni_1/*o*-CeO_2	-	-	-
9	Cu_1/*o*-CeO_2	-	-	-
10	Fe_1/*o*-CeO_2	-	-	-
11	Ru_1/*o*-CeO_2-ov	99.9	96.3	96.3
12	Ru_1/*c*-CeO_2-ov	80.7	84.9	68.5
13	Ru_1/*r*-CeO_2-ov	92.1	80.2	73.9

Reaction conditions: 1 mmol **1a**, 0.3 mol% metal-based catalyst, 3 mL *n*-octane, 100 °C, 3 MPa H_2, 3 h. [a] cis- and trans- 2-MCH. [b] 30 mg catalyst.

hydrogenation of **1a** to **2a** is the main route of the reaction network, while the demethoxylation reaction of **2a** is more difficult to occur [Figure 3D].

Condition optimization and catalyst stability

According to the results of the previous single-factor investigation experiment [Supplementary Figure 14], a three-factor, three-level response surface experiment model was set up [Supplementary Table 1]. Design-Expert 13 was used to analyze the obtained data [Supplementary Table 2]. It could be seen that the P value of the model was less than 0.0001, R^2 = 0.988, and the adjusted R^2 = 0.974, all of which were above 90%, indicating that the model's fit had a minor error with the actual situation and could better use the response value to analyze each factor. From the response surface of temperature-time (AB) parameters to predict the yield of **2a** [Figure 4A], it could be seen that the yield of **2a** also increased with the temperature due to the influence of kinetics. However, the high reaction temperature (> 100 °C) decreased the yield of **2a**, mainly due to the accelerated demethoxylation reaction of **2a** at a high temperature. Similarly, due to the continuous conversion of **2a** to **3a**, the effect of reaction time on the yield of **2a** also showed a volcano-shaped curve trend. The response surface of temperature-pressure (AC) parameters and time-pressure (BC) parameters for predicting the yield of **2a** found that a too-high pressure did not increase the yield of **2a** [Figure 4B and C]. One primary reason was that excessive hydrogen coverage would change the electrostatic interactions between hydrogen atoms and reaction intermediates, thus affecting the **2a** selectivity. The 3D surface plot showed that compared with the relatively gentle AC and BC surfaces, the AB surface (P = 0.0003) was steeper, which meant that temperature and time had a relatively more significant impact on the yield of **2a**. The 2D contour map corresponding to the surface showed that the lowest value of the **2a** yield contour under the AB parameter was below 50%, which was significantly lower than that under the AC and BC parameters, further proving the sensitivity of the temperature-time parameters to the **2a** yield [Figure 4D-F]. Similarly, analysis of the P values of the three single factors revealed that temperature (P < 0.0001) and time (P < 0.0002) had a more significant impact on the yield of **2a** than hydrogen pressure (P = 0.0026). Finally, according to the results of response surface prediction, the highest **2a** yield reached

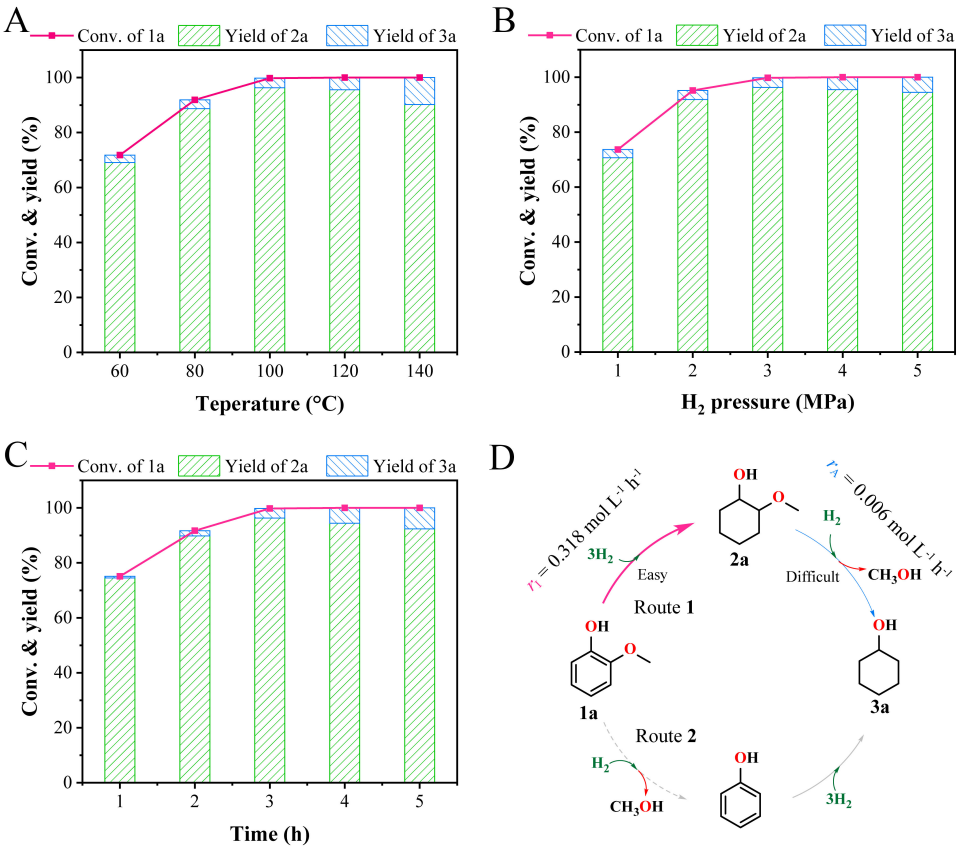

Figure 3. Reaction network analysis of **1a**. Effects of temperature (A); hydrogen pressure (B); and time (C) on the **1a** conversion and product yield; (D) Proposed **1a** reaction network, where Route **1** is that **1a** undergoes aromatic ring hydrogenation to generate **2a** followed by C-O bond cleavage, while Route **2** involves the first C-O bond cleavage and then the dearomatization process. Reaction conditions: 1 mmol **1a**, Ru_1/o-CeO_2-ov of 0.3 mol% Ru, 3 mL *n*-octane.

97.1% under the conditions of 120 °C, 2.3 h, and 3.4 MPa H_2.

After 2 h of reaction, Ru_1/o-CeO_2-ov was removed from the reaction system to verify the catalyst's heterogeneous behavior [Figure 4G]. ICP-OES analysis of the liquid mixture after the reaction revealed no Ru signal, which means that the metallic Ru on the catalyst was not leached into the reaction solution [Supplementary Figure 15]. The yield of **2a** did not increase with the continuous increase of reaction time, illustrating that the catalytic reaction is heterogeneous. After the recovered catalyst was reused five times, the conversion rate of **1a** only decreased by 9%, and the activity of the reused catalyst could be completely recovered after reduction [Figure 4H]. According to the ICP test results, the Ru content of the used Ru_1/o-CeO_2-ov was 0.281 *wt*%, which is consistent with the mass fraction of Ru in the fresh Ru_1/o-CeO_2-ov (0.287 *wt*%). The XRD patterns of the used catalyst exhibited diffraction peaks consistent with those of the fresh counterpart, with no new diffraction peaks appearing [Supplementary Figure 16]. HAADF STEM image and EDS mappings showed that the used catalyst maintained a good octahedral morphology and that the metal Ru did not agglomerate [Figure 4I]. Therefore, the Ru_1/o-CeO_2-ov catalyst can maintain good activity and recyclability in the hydrogenation of **1a**.

Mechanism study

To explore the effect of the crystal plane structure of ceria on the hydrogenation of aromatic rings, models of single-atom Ru loaded on the (111), (100), and (110) planes of CeO_2 containing oxygen vacancies were

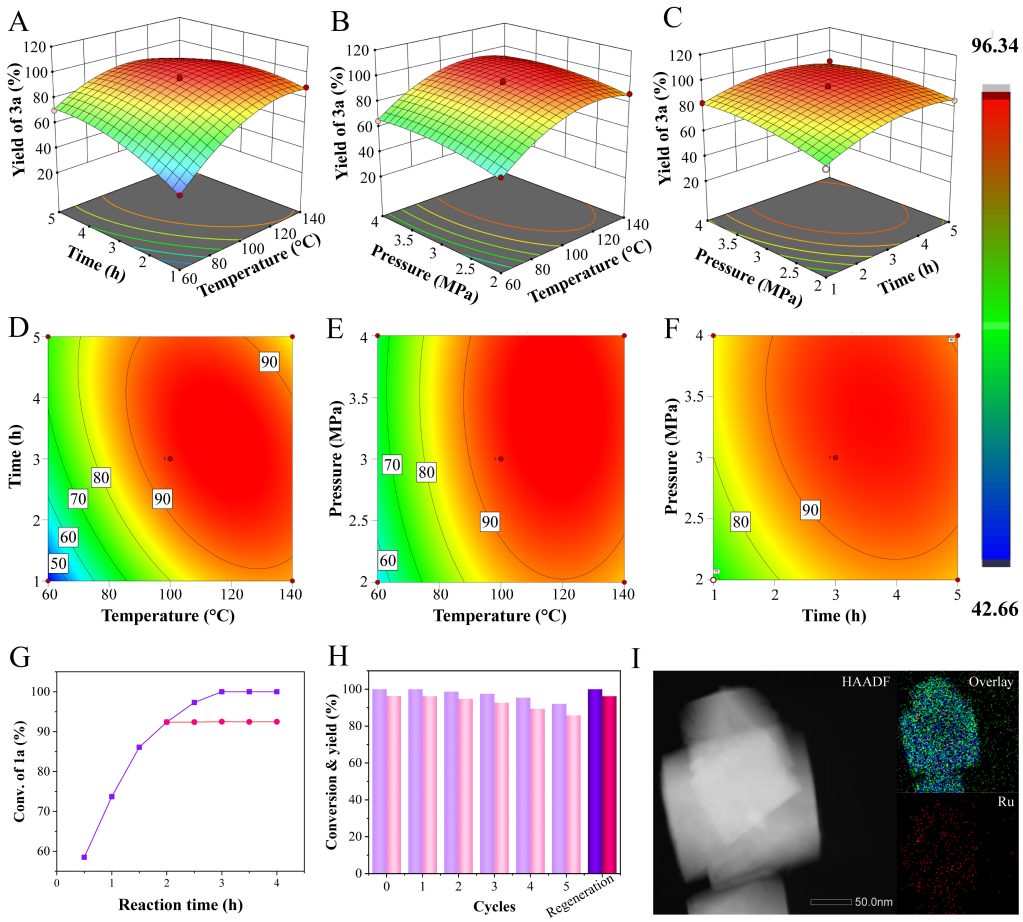

Figure 4. Data from response surface optimization and catalyst stability. The 3D surfaces show the effects of temperature-time (A); temperature-pressure (B), and time-pressure (C) parameters on the yield of **2a**; The 2D contours show the effects of temperature-time (D); temperature-pressure (E); and time-pressure (F) parameters on the yield of **2a**; (G) Heterogeneous catalytic behavior of Ru_1/o-CeO_2-ov catalyst (Reaction conditions: 1 mmol **1a**, 0.3 mol% Ru_1/o-CeO_2-ov, 3 mL *n*-octane, 100 °C, 3 MPa H_2); (H) Ru_1/o-CeO_2-ov catalyst recycling study (Reaction conditions: 0.3 mol% Ru_1/o-CeO_2-ov for **1a**, 3 mL *n*-octane, 100 °C, 3 MPa H_2, 3 h; Regeneration conditions refer to the process of preparing Ru_1/o-CeO_2-ov from Ru_1/o-CeO_2); (I) HAADF STEM image and EDS mappings of the Ru_1/o-CeO_2-ov catalyst after use. 2D: Two-dimensional; 3D: three-dimensional; HAADF STEM: high-angle annular dark field scanning transmission electron microscope; EDS: energy-dispersive X-ray spectrometer.

established and optimized, corresponding to Ru_1/o-CeO_2-ov, Ru_1/c-CeO_2-ov, and Ru_1/r-CeO_2-ov, respectively [Figure 5A]. It was generally believed that the opening of the π bond of the aromatic ring, that was, the addition of the first hydrogen atom, was the rate-determining step of hydrogenation saturation, which means that the first step in the entire saturation process requires the highest energy[45,46]. Therefore, we calculated the energetics of the first-step hydrogenation of the aromatic ring in **1a** to compare the hydrogenation performance of catalysts with different preferentially exposed crystal planes. As shown in Figure 5B-D, the Ru_1/o-CeO_2-ov catalyst represented by the CeO_2(111) plane only needs to overcome an energy barrier of 0.22 eV to complete the hydrogenation of the aromatic ring. However, the catalysts represented by the (100) and (110) planes need to overcome 0.34 eV and 0.30 eV, respectively, indicating that guaiacol was more likely to complete the aromatic ring hydrogenation reaction over the Ru_1/o-CeO_2-ov catalyst from a kinetic point of view. The above conclusions explain well that the Ru_1/o-CeO_2-ov catalyst activity prepared with octahedral ceria in the experiment is better than that of cubic and rod-shaped ceria.

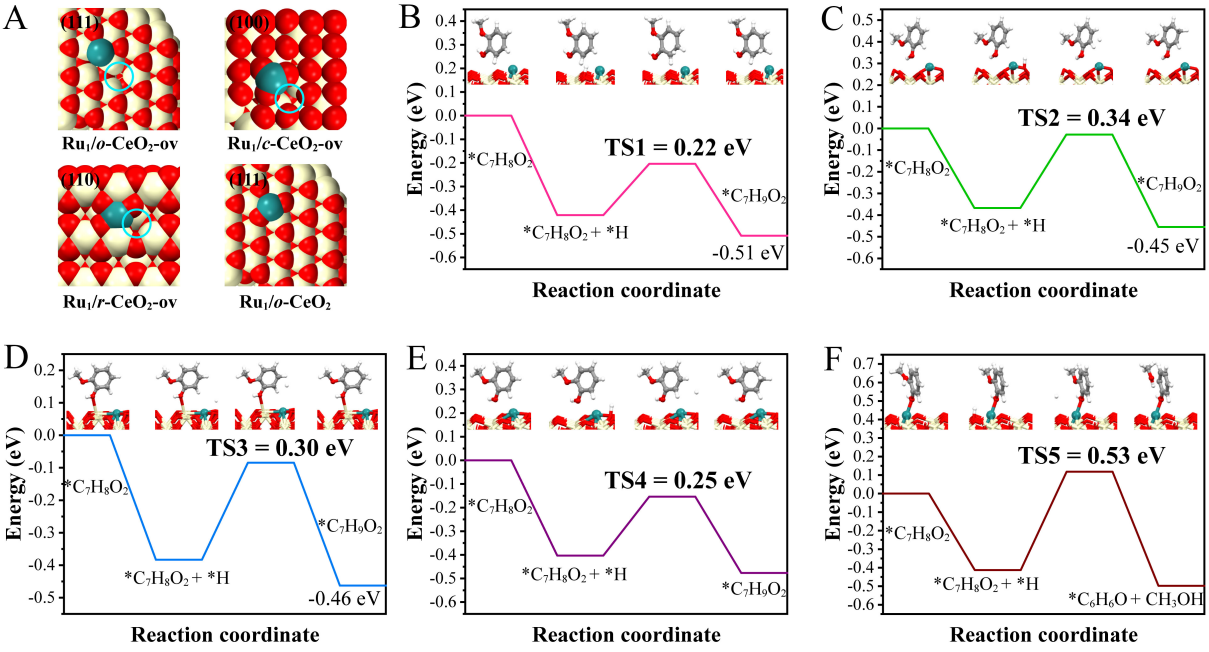

Figure 5. Mechanism study. (A) Models of single-atom Ru supported on different crystal planes of ceria with and without oxygen vacancies. Transition state energy barriers of **1a** hydrogenation over single-atom Ru catalysts containing oxygen vacancies on the (111) (B), (100) (C), and (110) (D) planes; (E) Transition state energy barriers of **1a** hydrogenation on a single-atom Ru catalyst without oxygen vacancies on the (111) plane; (F) Transition state energy barriers of C_{Ar}-OCH_3 bond cleavage of **1a** over Ru_1/o-CeO_2-ov catalyst.

To investigate the effect of ceria oxygen vacancies on the hydrogenation of **1a** and the superior selectivity of Ru_1/o-CeO_2-ov catalyst toward **2a**, the energy of aromatic ring hydrogenation on the catalyst corresponding to intact CeO_2(111) plane was calculated [Figure 5E]. It could be seen that the transition state energy (0.25 eV) generated at the Ru_1/o-CeO_2 site was lower than that of the Ru_1/o-CeO_2-ov catalyst, indicating that the ceria oxygen vacancies on the catalyst surface will promote the aromatic ring hydrogenation reaction. Subsequently, when calculating the demethoxylation reaction energy of **1a** [Figure 5F], it was found that the energy for the Ru_1/o-CeO_2-ov active site to complete the C_{Ar}-OCH_3 bond cleavage was 0.53 eV, which was 2.4 times that of the aromatic ring hydrogenation, suggesting that it was difficult for the Ru_1/o-CeO_2-ov catalyst to complete the reaction at low energy, further explaining the high **2a** selectivity of the catalyst.

Substrate range

Thanks to the 100% utilization of single-atom Ru metal and the Ru-O-Ce active sites rich in oxygen vacancies, Ru_1/o-CeO_2-ov had a relatively high TOF = 107 h^{-1} compared with several metal catalysts reported in the literature [Figure 6A][25,27,28,30,47,48]. Subsequently, the aromatic ring hydrogenation performance of a series of lignin-derived phenols was evaluated using Ru_1/o-CeO_2-ov catalyst [Figure 6B]. The yields of the corresponding hydrogenated products of the guaiacol derivatives (**1a-1d**) obtained after the reaction could reach a good level (88%-96%). Surprisingly, since phenol derivatives were not affected by methoxy groups, the yields of the corresponding hydrogenated products could reach over 96% (**2e-2h**). The aromatic ring could also reach complete saturation when using syringyl 2,6-dimethoxyphenol (**1i**) as a substrate. Unfortunately, because higher temperatures were required to activate the aromatic ring in **1i**, more than 60% of the product was a mixture of **2a** (46% yield) and **2e** (15% yield), and the corresponding hydrogenation product **2i** was only 31%. Finally, the aromatic ring hydrogenation performance of Ru_1/o-CeO_2-ov catalyst was investigated using real lignin oil from birch wood hydrogenolysis. In the 2D HSQC NMR spectrum of lignin oil, three signal regions of δ(C)/δ(H) = 100-140/5.5-8.0 [Figure 6C],

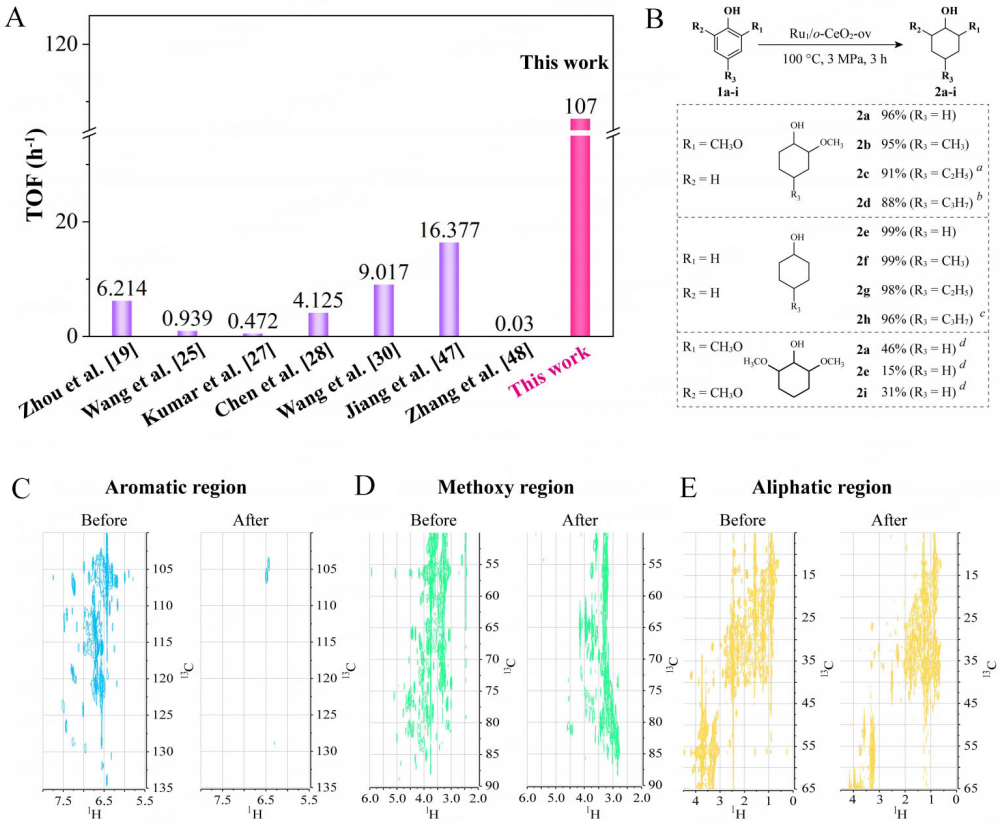

Figure 6. (A) TOF comparison of **1a** hydrogenation reaction on Ru_1/o-CeO_2-ov and literature catalysts; (B) Hydrogenation performance of different lignin-derived phenols catalyzed by Ru_1/o-CeO_2-ov ([a] 150 °C; [b] 160 °C, 4 h; [c] 4 h; [d] 200 °C, 3 MPa H_2, 4 h); 2D HSQC NMR spectra of authentic lignin oil in the aromatic region (C); methoxy region (D), and aliphatic region (E) before and after the reaction. 2D HSQC NMR: Two-dimensional heteronuclear single quantum coherence nuclear magnetic resonance.

δ(C)/δ(H) = 50-90/2.0-6.0 [Figure 6D], and δ(C)/δ(H) = 0-65/0.5-4.0 [Figure 6E] are observed, corresponding to the aromatic, methoxy, C-C aliphatic and regions, respectively. Compared with the lignin oil raw material, the 2D HSQC NMR spectra of the product showed that the aromatic region signal of δ(C)/δ(H) = 90-140/5.5-8.0 disappears, which meant that most of the aromatic rings in the lignin oil had been hydrogenated [Figure 6C]. Excitingly, a large number of signals still existed in the methoxy region of the product [Figure 6D], confirming that the methoxy groups in the lignin oil were retained, which demonstrates that the Ru_1/o-CeO_2-ov catalyst had excellent aromatic ring hydrogenation ability while inhibiting the cleavage of the C-O bond.

CONCLUSIONS

In summary, we developed a versatile catalytic strategy to rapidly hydrogenate the aromatic ring of guaiacols while suppressing C-O bond cleavage by tuning the crystal plane of the ceria and the oxygen vacancies of the Ru_1/o-CeO_2-ov catalyst. The Ru_1/o-CeO_2-ov catalyst had excellent aromatic ring hydrogenation ability due to the formation of Ru-O-Ce active sites. DFT calculations elaborated that the oxygen vacancies and preferentially exposed (111) plane of ceria could reduce the transition state energy barrier of aromatic ring hydrogenation, which was only 40% of the C_{Ar}-OCH_3 bond cleavage energy. Response surface experiment optimization revealed that temperature and time were more sensitive to the selectivity of the target product than hydrogen pressure, and the yield of 2-MCH could exceed 97% under the optimal process conditions. The Ru_1/o-CeO_2-ov catalyst was able to completely hydrogenate almost all

lignin-derived phenols, including real lignin oil, which provides a new application direction for CeO_2 crystal surface regulation, namely, the transformation of lignin-derived phenols into value-added chemicals.

DECLARATIONS

Authors' contributions

Experimentation: Wang, B.
Writing - review and editing: Wang, B.; Yan, X.; Li, H.
Investigation: Wang, B.; Yan, X.; Zhou, M.
Methodology: Wang, B.; Yan, X.; Zhou, M.; Li, H.
Formal analysis: Wang, B.; Yan, X.
Supervision, conceptualization: Li, H.

Availability of data and materials

The related data, deposited in the individual repositories of the participating institutions, will be provided upon request.

Financial support and sponsorship

The authors acknowledge the financial support from the National Natural Science Foundation of China (52466011, 22368014, 22478087), Marine Science First-Class Subject, Beibu Gulf University, Natural Science Foundation of Guangxi Zhuang Autonomous Region (2024GXNSFAA010382, 2025GXNSFAA069590), and Guizhou Provincial S&T Project (GCC [2023]011, ZK [2022]011).

Conflicts of interest

Li, H. is the Guest Editor of the Special Issue of "Biofuels and Carbon Resource Utilization" of the journal of *Energy Materials* and was not involved in any steps of editorial processing, notably including reviewer selection, manuscript handling, or decision making. The other authors declare that there are no conflicts of interest.

Ethical approval and consent to participate

Not applicable.

Consent for publication

Not applicable.

REFERENCES

1. Ashokkumar, V.; Venkatkarthick, R.; Jayashree, S.; et al. Recent advances in lignocellulosic biomass for biofuels and value-added bioproducts - a critical review. *Bioresour. Technol.* **2022**, *344*, 126195. DOI
2. Pompei, S.; Grimm, C.; Schiller, C.; Schober, L.; Kroutil, W. Thiols act as methyl traps in the biocatalytic demethylation of guaiacol derivatives. *Angew. Chem. Int. Ed.* **2021**, *60*, 16906-10. DOI PubMed PMC
3. Smet G, Bai X, Maes BUW. Selective C(aryl)-O bond cleavage in biorenewable phenolics. *Chem. Soc. Rev.* **2024**, *53*, 5489-551. DOI PubMed
4. Zhao, Y.; Zhan, J.; Hu, R.; et al. Water-assisted catalytic transfer hydrogenation of guaiacol to cyclohexanol over Ru/$NiAl_2O_4$. *Chem. Eng. J.* **2024**, *485*, 149934. DOI
5. Wang, B.; Huang, J.; Wu, H.; Yan, X.; Liao, Y.; Li, H. Synergy of heterogeneous Co/Ni dual atoms enabling selective C-O bond scission of lignin coupling with in-situ N-functionalization. *J. Energy. Chem.* **2024**, *92*, 16-25. DOI
6. Smet G, Bai X, Mensch C, Sergeyev S, Evano G, Maes BUW. Selective nickel-catalyzed hydrodeacetoxylation of aryl acetates. *Angew. Chem. Int. Ed.* **2022**, *61*, e202201751. DOI PubMed

7. Wu, R.; Meng, Q.; Yan, J.; et al. Intermetallic synergy in platinum-cobalt electrocatalysts for selective C-O bond cleavage. *Nat. Catal.* **2024**, *7*, 702-18. DOI
8. Lang, M.; Li, H. Toward value-added arenes from lignin-derived phenolic compounds via catalytic hydrodeoxygenation. *ACS. Sustainable. Chem. Eng.* **2022**, *10*, 13208-43. DOI
9. Zhang, J.; Sun, J.; Wang, Y. Recent advances in the selective catalytic hydrodeoxygenation of lignin-derived oxygenates to arenes. *Green. Chem.* **2020**, *22*, 1072-98. DOI
10. Lang, M.; Li, H. Heterogeneous metal-based catalysts for cyclohexane synthesis from hydrodeoxygenation of lignin-derived phenolics. *Fuel* **2023**, *344*, 128084. DOI
11. Wong, S. S.; Shu, R.; Zhang, J.; Liu, H.; Yan, N. Downstream processing of lignin derived feedstock into end products. *Chem. Soc. Rev.* **2020**, *49*, 5510-60. DOI
12. Winterton, N. The green solvent: a critical perspective. *Clean. Technol. Environ. Policy.* **2021**, *23*, 2499-522. DOI PubMed PMC
13. Marco-Contelles, J.; Molina, M. T.; Anjum, S. Naturally occurring cyclohexane epoxides: sources, biological activities, and synthesis. *Chem. Rev.* **2004**, *104*, 2857-900. DOI PubMed
14. Liu, L.; Liu, L.; Zhang, K.; et al. Selective conversion of cyclohexene to 2-methoxycyclohexanol over molybdenum oxide on beta zeolite. *Ind. Eng. Chem. Res.* **2023**, *62*, 16207-14. DOI
15. Feng, J.; Shang, Y.; Zhang, Y. Research on synthesis and thermodynamic properties of 2-methoxycyclohexanol. *J. Therm. Anal. Calorim.* **2018**, *131*, 2197-203. DOI
16. Jiang, Y.; Huang, J.; Hunger, M.; Maciejewski, M.; Baiker, A. Comparative studies on the catalytic activity and structure of a Cu-MOF and its precursor for alcoholysis of cyclohexene oxide. *Catal. Sci. Technol.* **2015**, *5*, 897-902. DOI
17. Obeso, J. L.; Gabriel, F. J.; Flores, C. V.; et al. Lewis acid-catalyzed ring-opening alcoholysis of cyclohexene oxide: the role of open metal sites in the Bi(III)□based metal-organic framework SU-101. *ChemCatChem* **2023**, *15*, e202300471. DOI
18. Abbasi, K. R.; Shahbaz, M.; Zhang, J.; Irfan, M.; Alvarado, R. Analyze the environmental sustainability factors of China: the role of fossil fuel energy and renewable energy. *Renew. Energy.* **2022**, *187*, 390-402. DOI
19. Zhou, H.; Wang, H.; Sadow, A. D.; Slowing, I. I. Toward hydrogen economy: Selective guaiacol hydrogenolysis under ambient hydrogen pressure. *Appl. Catal. B. Environ.* **2020**, *270*, 118890. DOI
20. Nakagawa, Y.; Ishikawa, M.; Tamura, M.; Tomishige, K. Selective production of cyclohexanol and methanol from guaiacol over Ru catalyst combined with MgO. *Green. Chem.* **2014**, *16*, 2197-203. DOI
21. Hensley, A. J.; Bray, J.; Shangguan, J.; Chin, Y. H.; Mcewen, J. S. Catalytic consequences of hydrogen addition events and solvent-adsorbate interactions during guaiacol-H_2 reactions at the H_2O-Ru(0001) interface. *J. Catal.* **2021**, *395*, 467-82. DOI
22. Wang, B.; Zhou, P.; Yan, X.; Li, H.; Wu, H.; Zhang, Z. Cooperative catalysis of Co single atoms and nanoparticles enables selective CAr-OCH_3 cleavage for sustainable production of lignin-based cyclohexanols. *J. Energy. Chem.* **2023**, *79*, 535-49. DOI
23. Nania, C.; Bertini, M.; Gueci, L.; Ferrante, F.; Duca, D. DFT insights into competing mechanisms of guaiacol hydrodeoxygenation on a platinum cluster. *Phys. Chem. Chem. Phys.* **2023**, *25*, 10460-71. DOI PubMed
24. Zhang, K.; Meng, Q.; Wu, H.; et al. Selective hydrodeoxygenation of aromatics to cyclohexanols over ru single atoms supported on CeO_2. *J. Am. Chem. Soc.* **2022**, *144*, 20834-46. DOI
25. Wang, X.; Zhu, S.; Wang, S.; Wang, J.; Fan, W.; Lv, Y. Ni nanoparticles entrapped in nickel phyllosilicate for selective hydrogenation of guaiacol to 2-methoxycyclohexanol. *Appl. Catal. A. Gen.* **2018**, *568*, 231-41. DOI
26. Yamaguchi, A.; Murakami, Y.; Yamazaki, K.; Shirai, M.; Hiyoshi, N. Stereoselective hydrogenation of guaiacol to cis-2-methoxycyclohexanol using supported rhodium catalysts in supercritical carbon dioxide. *Catal. Today.* **2024**, *425*, 114356. DOI
27. Kumar, A.; Kumar, J.; Bhaskar, T. High surface area biochar from sargassum tenerrimum as potential catalyst support for selective phenol hydrogenation. *Environ. Res.* **2020**, *186*, 109533. DOI PubMed
28. Chen, J.; Ji, J.; Tu, T. Selective hydrogenation of phenols to cyclohexanols catalyzed by robust solid NHC-Rh coordination assemblies in water. *Green. Chem.* **2023**, *25*, 7541-6. DOI
29. Qian, W.; Lin, L.; Qiao, Y.; et al. Ru subnanoparticles on N-doped carbon layer coated SBA-15 as efficient Catalysts for arene hydrogenation. *Appl. Catal. A. Gen.* **2019**, *585*, 117183. DOI
30. Wang, Q.; De, B. M. C. M.; Safonova, O. V.; et al. Tunable catalysis by reversible switching between $Ru_{(III)}$ single sites and Ru_0 clusters in solid micelles. *J. Catal.* **2023**, *426*, 336-44. DOI
31. Wang, A.; Li, J.; Zhang, T. Heterogeneous single-atom catalysis. *Nat. Rev. Chem.* **2018**, *2*, 65-81. DOI
32. Li, L.; Chang, X.; Lin, X.; Zhao, Z. J.; Gong, J. Theoretical insights into single-atom catalysts. *Chem. Soc. Rev.* **2020**, *49*, 8156-78. DOI
33. Gong, X.; Song, P.; Han, C.; Xiao, Y.; Mei, X.; Xu, W. Heterogeneous single-atom catalysts for energy process: recent progress, applications and challenges. *Energy. Mater.* **2023**,. DOI
34. Wang, W.; Li, S.; Qiang, Q.; et al. Catalytic refining lignin-derived monomers: seesaw effect between nanoparticle and single-atom Pt. *Angew. Chem. Int. Ed.* **2024**, *63*, e202404683. DOI
35. Zhang, L.; Shang, N.; Gao, S.; et al. Atomically dispersed Co catalyst for efficient hydrodeoxygenation of lignin-derived species and hydrogenation of nitroaromatics. *ACS. Catal.* **2020**, *10*, 8672-82. DOI
36. Li, J.; Ge, J.; Zhao, Y.; et al. Lignin-tailored fabrication of Ni single atom catalyst with Ni-N_3 active site for efficient and selective catalytic transfer hydrogenation of lignin-derived aldehydes. *Chem. Eng. J.* **2024**, *496*, 154315. DOI
37. Guo, H.; Zhao, J.; Chen, Y.; et al. Mechanistic insights into hydrodeoxygenation of lignin derivatives over Ni single atoms supported

on Mo_2C. *ACS. Catal.* **2024**, *14*, 703-17. DOI

38. Gao, X.; Ma, R.; Liu, Z.; Wang, S.; Wu, Y.; Song, G. Hydrodeoxygenation of lignin-derived phenols into cycloalkanes by atomically dispersed Pt-polyoxometalate catalysts. *Appl. Catal. B. Environ. Energy.* **2024**, *352*, 124059. DOI
39. Jiang, F.; Wang, S.; Liu, B.; et al. Insights into the influence of CeO_2 crystal facet on CO_2 hydrogenation to methanol over Pd/CeO_2 catalysts. *ACS. Catal.* **2020**, *10*, 11493-509. DOI
40. Li, H.; Zha, S.; Zhao, Z.; et al. The nature of loading-dependent reaction barriers over mixed RuO_2/TiO_2 catalysts. *ACS. Catal.* **2018**, *8*, 5526-32. DOI
41. Huang, H.; Dai, Q.; Wang, X. Morphology effect of Ru/CeO_2 catalysts for the catalytic combustion of chlorobenzene. *Appl. Catal. B. Environ.* **2014**, *158-159*, 96-105. DOI
42. Campbell, C. T.; Peden, C. H. Oxygen vacancies and catalysis on ceria surfaces. *Science* **2005**, *309*, 713-4. DOI PubMed
43. Vayssilov, G. N.; Lykhach, Y.; Migani, A.; et al. Support nanostructure boosts oxygen transfer to catalytically active platinum nanoparticles. *Nat. Mater.* **2011**, *10*, 310-5. DOI
44. Liu, P.; Zheng, C.; Liu, W.; Wu, X.; Liu, S. Oxidative redispersion-derived single-site Ru/CeO_2 catalysts with mobile Ru complexes trapped by surface hydroxyls instead of oxygen vacancies. *ACS. Catal.* **2024**, *14*, 6028-44. DOI
45. Zhao, Z.; Bababrik, R.; Xue, W.; et al. Solvent-mediated charge separation drives alternative hydrogenation path of furanics in liquid water. *Nat. Catal.* **2019**, *2*, 431-6. DOI
46. Arora, S. S.; Bhan, A. Kinetics of aromatics hydrogenation on HBEA. *J. Catal.* **2020**, *383*, 24-32. DOI
47. Jiang, W.; Cao, J.; He, Z.; et al. Highly selective hydrogenation of arenes over Rh nanoparticles immobilized on α-Al_2O_3 support at room temperature. *Chem. Eng. Sci.* **2023**, *270*, 118544. DOI
48. Zhang, Q.; Li, H.; Gao, P.; Wang, L. PVP-NiB amorphous catalyst for selective hydrogenation of phenol and its derivatives. *Chin. J. Catal.* **2014**, *35*, 1793-9. DOI